

NASA Technical Memorandum 83548
AIAA-84-0531



Computation of Viscous Flow in Curved Ducts and Comparison With Experimental Data

(NASA TM-83548) COMPUTATION OF VISCOUS FLOW
IN CURVED DUCTS AND COMPARISON WITH
EXPERIMENTAL DATA (NASA) 22 p HC A02/MF A01
CSCL 20D

N84-13494

G3/34 42739
Unclass

Charles E. Towne
*Lewis Research Center
Cleveland, Ohio*

Prepared for the
Twenty-second Aerospace Sciences Meeting
sponsored by the American Institute of
Aeronautics and Astronautics
Reno, Nevada, January 9-12, 1984

NASA

COMPUTATION OF VISCOUS FLOW IN CURVED DUCTS AND COMPARISON

WITH EXPERIMENTAL DATA

Charles E. Towne

National Aeronautics and Space Administration
Lewis Research Center
Cleveland, Ohio 44135

SUMMARY

A three-dimensional analysis for fully viscous subsonic internal flow is evaluated. The analysis, designated PEP SIG, solves an approximate form of the Navier-Stokes equations by an implicit spatial marching procedure. Results of calculations are presented for laminar flow through two different circular cross-sectioned 180 degree bends, and for laminar and turbulent flow through circular and square cross-sectioned 22.5-22.5 degree S-ducts. Quantitative comparisons with experimental data are shown for all cases. Special emphasis is placed on verifying the ability of the analysis to accurately predict the distorted flow fields resulting from pressure-driven secondary flows.

INTRODUCTION

The presence of three-dimensional subsonic internal flow is relatively common in many of today's airbreathing propulsion systems. Curved centerlines and changes in cross-sectional shape are often present, resulting in the generation of complex three-dimensional secondary flows and significant flow distortion. In addition, viscous effects are usually important, with the boundary layer thickness often comparable to the duct radius. These phenomena have important effects on overall propulsion system performance.

Conventional boundary layer methods will not work for these complex flows. A full Navier-Stokes solution could be used, but would require large amounts of computer time and storage. However, by making certain approximations to the Navier-Stokes equations, such as neglecting streamwise diffusion, a set of equations can be derived for fully viscous internal flow that can be solved by forward marching in space. An analysis method using these equations to compute three-dimensional subsonic flow through curved ducts with super-elliptic cross-sections was developed by Briley and McDonald (ref. 1) and by Levy, McDonald, Briley, and Kreskovsky (ref. 2), and was designated PEP SIG. A preliminary evaluation of the PEP SIG method was presented by Towne and Anderson (ref. 3). However, in that evaluation only qualitative comparisons were made with data. In addition, several changes have since been made to the analysis by Levy, Briley, and McDonald (ref. 4).

The objective of the present study, therefore, was to evaluate and verify the most recent version of the PEP SIG analysis by making detailed quantitative comparisons between predicted results and benchmark experimental data. Special emphasis was placed on testing the ability of the analysis to accurately predict the distorted flow field resulting from pressure-driven secondary flows.

GOVERNING EQUATIONS

In this analysis, the flow is computed by a single sweep spatial marching procedure which solves an approximate form of the Navier-Stokes equations. It is assumed that the flow is primarily in the direction of the duct centerline, with transverse secondary flow. This allows two basic assumptions to be made. The first is that second derivatives in the primary flow direction are negligible. The second is that the pressure in the primary, or streamwise, momentum equation can be represented by the sum of a known three-dimensional pressure field and a one-dimensional correction computed as part of the marching procedure to account for viscous blockage. When these two assumptions are applied to the Navier-Stokes equations, a set of equations can be derived that can be solved by forward marching in the primary flow direction.

The details of the derivation of the governing equations have been presented elsewhere (refs. 1, 2, and 4). For completeness, however, a brief discussion is presented here. The equations are first written in a centerline-based orthogonal reference coordinate system denoted by x_1 , x_2 , and x_3 , with corresponding velocities v_s , w_s , and u_p . The x_3 direction is the primary flow direction, and is aligned with the duct centerline at each marching step. The x_1 and x_2 directions are normal to the duct centerline and define the transverse, or secondary, flow plane. The primary momentum equation is then given by

$$\begin{aligned} \frac{\rho u_p}{h} \frac{\partial u_p}{\partial x_3} + \rho v_s \frac{\partial u_p}{\partial x_1} + \rho w_s \frac{\partial u_p}{\partial x_2} + \frac{\rho u_p v_s}{h} \frac{\partial h}{\partial x_1} + \frac{\rho u_p w_s}{h} \frac{\partial h}{\partial x_2} &= \frac{1}{h} \frac{\partial}{\partial x_3} (p_i + p_v) \\ &+ \frac{1}{h} \frac{\partial}{\partial x_1} \left(h \mu \frac{\partial u_p}{\partial x_1} - \mu u_p \frac{\partial h}{\partial x_1} \right) + \frac{1}{h} \frac{\partial}{\partial x_2} \left(h \mu \frac{\partial u_p}{\partial x_2} - \mu u_p \frac{\partial h}{\partial x_2} \right) \\ &+ \frac{\mu}{h} \frac{\partial h}{\partial x_1} \frac{\partial u_p}{\partial x_1} - \frac{\mu u_p}{h^2} \left(\frac{\partial h}{\partial x_1} \right)^2 + \frac{\mu}{h} \frac{\partial h}{\partial x_2} \frac{\partial u_p}{\partial x_2} - \frac{\mu u_p}{h^2} \left(\frac{\partial h}{\partial x_2} \right)^2 \end{aligned}$$

This equation, and the others to be presented in this section, are taken directly from reference 4. Here h is the metric scale coefficient associated with the primary direction x_3 . (The metric scale coefficients for the transverse directions are both unity). Also, $p_i = p_i(x_1, x_2, x_3)$ is the known three-dimensional pressure field and $p_v = p_v(x_3)$ is the unknown one-dimensional viscous blockage correction. In this study, p_i was computed using a three-dimensional potential flow analysis, thus bringing elliptic effects due to geometry into the solution.

The secondary velocities v_s and w_s are split into irrotational and rotational components. The continuity equation can then be written as

$$\frac{\partial}{\partial x_1} \left(\rho h \frac{\partial \phi}{\partial x_1} \right) + \frac{\partial}{\partial x_2} \left(\rho h \frac{\partial \phi}{\partial x_2} \right) + \frac{\partial}{\partial x_3} (\rho u_p) = 0$$

Here φ is a scalar potential corresponding to the irrotational component of the secondary velocity.

The transverse momentum equations are cross-differentiated and combined to form an equation for the transport of streamwise vorticity in the primary flow direction, given by

$$\begin{aligned} & \frac{\rho u_p}{h} \frac{\partial \Omega}{\partial x_3} + \frac{\partial}{\partial x_1} (\rho v_s \Omega) + \frac{\partial}{\partial x_2} (\rho w_s \Omega) + \frac{\partial w_s}{\partial x_3} \frac{\partial}{\partial x_1} \left(\frac{\rho u_p}{h} \right) - \frac{\partial v_s}{\partial x_3} \frac{\partial}{\partial x_2} \left(\frac{\rho u_p}{h} \right) \\ & - \frac{\partial}{\partial x_1} \left(\frac{\rho u_p^2}{h} \frac{\partial h}{\partial x_2} \right) + \frac{\partial}{\partial x_2} \left(\frac{\rho u_p^2}{h} \frac{\partial h}{\partial x_1} \right) + \frac{\partial \rho v_s}{\partial x_1} \frac{\partial v_s}{\partial x_2} - \frac{\partial \rho v_s}{\partial x_2} \frac{\partial v_s}{\partial x_1} + \frac{\partial \rho w_s}{\partial x_1} \frac{\partial w_s}{\partial x_2} \\ & - \frac{\partial \rho w_s}{\partial x_2} \frac{\partial w_s}{\partial x_1} - \frac{\partial}{\partial x_1} \left[\frac{1}{h} \frac{\partial}{\partial x_1} (h \mu \Omega) \right] - \frac{\partial}{\partial x_2} \left[\frac{1}{h} \frac{\partial}{\partial x_2} (h \mu \Omega) \right] = 0 \end{aligned}$$

where

$$v_s = v_\varphi + v_\psi = \frac{\partial \varphi}{\partial x_1} + \frac{1}{\rho h} \frac{\partial h \psi}{\partial x_2}$$

$$w_s = w_\varphi + w_\psi = \frac{\partial \varphi}{\partial x_2} - \frac{1}{\rho h} \frac{\partial h \psi}{\partial x_1}$$

Here ψ is the stream function, or vector potential, corresponding to the rotational component of the secondary velocity, and Ω is the vorticity in the x_3 direction.

The fourth equation is simply the definition of Ω written in terms of ψ .

$$\frac{\partial}{\partial x_1} \left(\frac{1}{\rho h} \frac{\partial h \psi}{\partial x_1} \right) + \frac{\partial}{\partial x_2} \left(\frac{1}{\rho h} \frac{\partial h \psi}{\partial x_2} \right) + \Omega = 0$$

The energy equation is eliminated by assuming constant total enthalpy. For turbulent flow, an algebraic mixing length turbulence model is used.

The above equations are transformed into a non-orthogonal body-fitted coordinate system. They are then solved by forward marching in the streamwise direction from an initial station, where the flow profiles are known, by an implicit finite-difference technique. The boundary conditions that are applied result in no-slip at the walls, and symmetry at the symmetry plane. Details of the solution procedure can be found in references 1, 2, and 4.

COMPUTED RESULTS

The results of the PEP SIG analysis have been compared with experimental data for a variety of geometric configurations and flow conditions. In this

section, results are presented and discussed for the following cases: (1) incompressible laminar flow through two different circular cross-sectioned 180 degree bends tested by Agrawal, Talbot, and Gong (ref. 5); (2) incompressible laminar and turbulent flow through a circular cross-sectioned 22.5-22.5 S-duct tested by Taylor, Whitelaw, and Yianneskis (ref. 6); and (3) incompressible laminar and turbulent flow through a square cross-sectioned 22.5-22.5 S-duct also tested by Taylor, Whitelaw, and Yianneskis (ref. 7). All of these data are of benchmark quality, with streamwise and cross-flow velocities measured using laser-doppler velocimetry. PEP SIG results for other configurations are presented by Anderson (ref. 8) and by Vakili, et al. (ref. 9).

180 Degree Bend

The two geometries tested in reference 5 are shown in figure 1. Both have a cross-section radius r of 1.905 cm (0.75 in.). They had centerline radii R of 13.335 cm (5.25 in.) and 38.1 cm (15.0 in.), corresponding to radius ratios R/r of 7 and 20, respectively.

$R/r = 7$. - The first results to be presented are for the $R/r = 7$ bend. The flow was laminar, with a Reynolds number Re of 242 based on the cross-section radius r and the average velocity \bar{u} , corresponding to a Dean number De of 183. The Dean number is defined as $De = 2 Re \sqrt{r/R}$. With a 20x20 mesh in half the cross-section (taking advantage of symmetry), and 181 streamwise marching steps, 1.7 minutes of CPU time were needed on a Cray-1 computer.

The computed secondary flow pattern after 60 degrees of turning is shown in figure 2. Each arrow in this figure represents the direction and magnitude of the secondary velocity at the tail of the arrow. This is the classic pattern for flow in a curved pipe. The low energy flow near the wall migrates circumferentially away from the outside, or pressure side, of the bend and toward the inside, or suction side. The higher speed flow in the core region moves toward the outside of the bend due to centrifugal effects. A pair of counter-rotating vortices is thus established. This secondary flow pattern persists through the length of the duct.

The resulting flow distortion is shown in figure 3 in the form of contours of constant streamwise velocity. These results are presented at the same stations used in the experiment. The boundary layer initially thickens slightly on the outside of the bend due to the pressure increase there as the flow enters the bend. By the second station, at 30 degrees, the effect of the secondary flow is apparent in the thickening of the boundary layer on the inside of the bend. By 60 degrees of turning the secondary flow has caused significant flow distortion. A pocket of low speed flow has formed on the inside of the bend, displacing the region of maximum velocity toward the outside of the bend. The results at the final two stations are similar.

In the experiment of reference 5, data were taken at five streamwise stations. At each station, streamwise velocity profiles were measured along the five data lines shown in the inset to figure 4. The computed streamwise velocity profiles along these data lines are compared with the data in figure 4. Computed results are shown for both 20x20 and 40x40 cross-sectional meshes; however, the effect of greater mesh resolution for this case is negligible.

For both meshes, the agreement between the PEP SIG results and the data is excellent.

The computed and experimental secondary velocity profiles are presented in figure 5. These results, both computed and experimental, are for slightly different flow conditions. The Reynolds and Dean numbers were 183 and 138, respectively. The distance between adjacent data lines in figure 5 corresponds to a v/\bar{u} value of 0.36. The agreement between theory and experiment is generally very good.

$R/r = 20$. - For the $R/r = 20$ case, the flow was laminar with a Reynolds number of 1263 and Dean number of 565. Several different meshes were used. For a $50 \times 50 \times 226$ mesh, 13.1 minutes of CPU time were used on a Cray-1 computer.

The computed secondary flow pattern after 84 degrees of turning is shown in figure 6. The basic pattern is similar to that seen in the $R/r = 7$ case, but the boundary layers are thinner, the secondary velocities are not as large, and the vortices are tighter. The computed streamwise velocity contours are shown in figure 7. Again, these results are qualitatively similar to those in the $R/r = 7$ case. However, the flow is more distorted, and becomes distorted after less turning.

In figures 8(a) and (b), the computed streamwise velocity profiles are compared with the data. (The results along data line 5 are not shown because of problems encountered in interpolating the computed results in the high velocity gradient region near the wall.) In figure 8(a), results for both 25×25 and 50×50 cross-sectional meshes are shown. A total of 226 points were used in the streamwise direction, with $\Delta\theta = 0.5$ degrees for θ between 0 and 45 degrees, and $\Delta\theta = 1.0$ degree for θ greater than 45 degrees. The agreement is generally very good for both meshes. In fact, the 25×25 mesh gives better results than the 50×50 mesh at $\theta = 108$ degrees. However, the coarser mesh is unable to resolve the velocity peak near the inner wall at $\theta = 35$ degrees seen along data lines 2 and 3. In figure 8(b), the results for the same $50 \times 50 \times 226$ mesh are shown along with results for a $50 \times 50 \times 181$ mesh with $\Delta\theta = 1.0$ degree for the entire duct. With the larger streamwise step size, the analysis is again unable to resolve the inner wall velocity peak at $\theta = 35$ degrees. These results indicate that proper mesh resolution in both the transverse and streamwise directions is critical in correctly predicting the initial development of the secondary flows.

Finally, in figure 9 the computed and experimental streamwise velocity contours are compared after 84 degrees of turning. The computed results are for the $50 \times 50 \times 226$ mesh. The agreement between theory and experiment is excellent.

Circular S-Duct

The circular cross-sectioned S-duct geometry tested in reference 6 consisted of two 22.5 degree circular arc bends, as shown in figure 10. The cross-section diameter D was 48 mm and the centerline radius R was 336 mm, for a ratio R/D of 7.

Laminar flow. - For the laminar flow case, the Reynolds number based on cross-section diameter D and average velocity \bar{u} was 790, corresponding to a Dean number of 211. With a 20x20x80 mesh, this case required 0.8 minutes of CPU time on a Cray-1 computer.

The computed secondary velocities near the inflection and exit planes are shown in figure 11. In the first bend the pressure-driven secondary flow pattern typical of curved pipes is set up. In the second bend, the cross-flow pressure gradients change sign, tending to attenuate the secondary flows set up in the first bend. In fact, by the time the exit plane is reached, a vortex-type motion has been set up in the lower half of the duct (i.e., near the inner wall of the second bend) that is in the opposite sense as that in the first bend. However, as noted in references 6, 7, and 10, the distortion of the streamwise flow in the first bend causes the generation of streamwise vorticity in the top half of the second bend that is in the same sense as that already present, in accordance with the Squire and Winter formula for the development of streamwise vorticity. The vortices set up in the first bend are thus sustained, or even intensified, in the second bend and become concentrated near the top of the duct.

The effect of the secondary flows on the streamwise flow is shown by the streamwise velocity contours in figure 12. The boundary layer along the bottom of the duct initially thickens due to the adverse pressure gradient there as the flow enters the duct. By the time the second station is reached, just ahead of the inflection plane, the secondary flows have caused the boundary layer in the top half of the duct to thicken significantly. Through the inflection region an adverse pressure gradient exists along the top of the duct, and the analysis predicts a small region of separated flow. This separation region has no appreciable effect on the rest of the flow, and the "FLARE" approximation (ref. 11) is used to allow the streamwise marching analysis to continue. In the second half of the duct the concentration of the vortices near the top causes a severely distorted flow field. In addition, the secondary velocities near the wall in the bottom half of the duct cause the boundary layer there to thicken. The flow at the duct exit is as distorted, or more distorted, than it would be in a unidirectional bend with the same total amount of turning.

In figure 13, the computed streamwise velocity profiles in the symmetry plane are compared with the data. Analytical results are shown for both 20x20x80 and 40x40x80 meshes. Both give very good agreement with the data, and the effect of greater mesh resolution is negligible.

Turbulent flow. - The Reynolds number for turbulent flow in the circular S-duct was 48,000, corresponding to a Dean number of 12,828. With a 50x50x80 mesh, this case required 4.8 minutes of CPU time on a Cray-1 computer.

The computed secondary velocities near the inflection and exit planes are shown in figure 14. The physical phenomena here are the same as in the laminar flow case. However, the boundary layers are much thinner, resulting in generally lower secondary velocities. The vortices are also somewhat more concentrated and nearer the top of the duct. The streamwise velocity contours are shown in figure 15. Again, except for the thinner boundary layers, these results are qualitatively similar to the laminar results.

In figure 16, the computed and experimental streamwise velocity profiles in the symmetry plane are compared with the data. In contrast to the laminar case, mesh resolution for the turbulent case has a significant effect on the results. With the 50x50x80 mesh, the PEP SIG results agree very well with the data. With the 25x25x80 mesh, however, the thin boundary layers and secondary flow vortices are not resolved well enough for the analysis to predict the distorted flow region at the top of the duct.

Square S-Duct

The square cross-sectioned S-duct geometry of reference 7 also consisted of two 22.5 degree circular arc bends, as shown in figure 10. The cross-section width D was 40 mm and the centerline radius R was 280 mm, for a ratio R/D of 7, the same as the circular cross-sectioned S-bend. Since the PEP SIG computer code is presently limited to super-elliptic cross-sections, the square cross-section was represented by a super-ellipse with an exponent of 10.

Laminar flow. - For the laminar flow case, the Reynolds number based on cross-section width D and average velocity \bar{u} was 790, corresponding to a Dean number of 211, the same as in the circular cross-sectioned laminar flow case. With a 20x20x111 mesh, this case required 1.2 minutes of CPU time on a Cray-1 computer.

The computed secondary velocities near the inflection and exit planes are shown in figure 17. The important physical phenomena for this case are the same as for the circular cross-sectioned case, and the secondary flow patterns are very similar. A pair of counter-rotating vortices is set up in the first bend. In the second bend, these vortices become concentrated near the top of the duct, and the near-wall secondary velocities in the lower half of the duct change direction.

The computed streamwise velocity contours are shown in figure 18. These results are, again, very similar to those in the circular cross-sectioned S-duct. In the first bend, the boundary layer in the top half of the duct thickens because of the secondary flows. In the second bend, the concentration of the vortices near the top of the duct again causes a severely distorted flow field. Small regions of separated flow were predicted for this case along the top of the duct near the inflection plane and along the bottom of the duct near the exit plane, where adverse pressure gradients exist.

The computed and experimental streamwise velocity profiles in the symmetry plane are compared in figure 19. Both the 20x20x111 and 40x40x111 mesh results agree very well with the data. The 20x20x111 case shows some undesirable wiggles, however, at the last two stations in the middle of the duct where the mesh resolution is poor.

Turbulent flow. - The Reynolds and Dean numbers for the turbulent flow case were 40,000 and 10,690, respectively. With a 50x50x111 mesh, this case required 7.7 minutes of CPU time on a Cray-1 computer.

The computed secondary velocities near the inflection and exit planes are shown in figure 20. As in the circular cross-sectioned case, these results are

basically similar to the corresponding laminar results, but with thinner boundary layers and generally lower secondary velocities. However, the vortices at the top of the duct have essentially disappeared by the time the exit plane is reached. In addition, in the second bend the streamwise velocity contours for turbulent flow, shown in figure 21, are shaped differently than for laminar flow. Near the top of the duct they have a gentle "W" shape, with the low speed flow extending furthest into the core region a short distance away from the symmetry plane. In the laminar flow case, in contrast, the low speed flow extended furthest into the core region exactly in the symmetry plane. The shape of these contour lines is in agreement with that found experimentally.

In figure 22 the computed and experimental streamwise velocity profiles in the symmetry plane are compared with the data. Computed results are shown for both 25x25x111 and 50x50x111 meshes. The 50x50x111 mesh gives slightly better agreement with the data than the 25x25x111 mesh, although the differences are small.

CONCLUDING REMARKS

For the configurations studied, the PEPSIG analysis gave quantitatively accurate results for both laminar and turbulent flow when sufficient mesh resolution was used. In particular, the analysis correctly predicted the complex physical phenomena and distorted flow fields that occur in S-shaped ducts. For the cases with thick inlet boundary layers, 20x20 cross-sectional meshes were sufficient. However, for the thin boundary layer cases a 50x50 cross-sectional mesh was generally needed for accurate results. Proper mesh resolution in both the transverse and streamwise directions was especially important in regions where the secondary flows were initially developing.

The PEPSIG analysis is very fast compared to the alternative, a full Navier-Stokes calculation. For the results presented in this paper, the current PEPSIG computer code processed 600-700 grid points per second on the Cray-1 computer. (The analysis is approximately 10 times slower on an IBM 370/3033). In reference 12, a time of 0.028 seconds per grid point per time step is reported for a three-dimensional problem solved by an efficient full Navier-Stokes procedure on an IBM 370/3033. Assuming 100 time steps for a converged solution, and a speed-up factor of 10 between the IBM and Cray, the Navier-Stokes procedure would process 3.6 grid points per second. The PEPSIG analysis is thus approximately 150-200 times faster, for comparable accuracy, than an efficient Navier-Stokes procedure.

REFERENCES

1. Briley, W. R., and McDonald, H., "Analysis and Computation of Viscous Subsonic Primary and Secondary Flows," AIAA Computational Fluid Dynamics Conference, Williamsburg, VA, July 1979, pp. 74-88.
2. Levy, R., McDonald, H., Briley, W. R., and Kreskovsky, J. P., "A Three-Dimensional Turbulent Compressible Subsonic Duct Flow Analysis for Use with Constructed Coordinate Systems," AIAA Paper 80-1398, July 1980.

3. Towne, Charles E., and Anderson, Bernhard H., "Numerical Simulation of Flows in Curved Diffusers with Cross-Sectional Transitioning Using a Three-Dimensional Viscous Analysis," AIAA Paper 81-0003, Jan. 1981.
4. Levy, R., Briley, W. R., and McDonald, H., "Viscous Primary/Secondary Flow Analysis for Use with Nonorthogonal Coordinate Systems," AIAA Paper 83-0556, Jan. 1983.
5. Agrawal, Y., Talbot, L., and Gong, K., "Laser Anemometer Study of Flow Development in Curved Circular Pipes," Journal of Fluid Mechanics, Vol. 85, Pt. 3, Apr. 13, 1978, pp. 497-518.
6. Taylor, A. M. K. P., Whitelaw, J. H., and Yianneskis, M., "Developing Flow in S-Shaped Ducts. II - Circular Cross-Section Duct," NASA CR-3759. To be published.
7. Taylor, A. M. K. P., Whitelaw, J. H., and Yianneskis, M., "Developing Flow in S-Shaped Ducts. I - Square Cross-Section Duct," NASA CR-3550, May 1982.
8. Anderson, B. H., "Three-Dimensional Viscous Design Methodology for Advanced Technology Aircraft Supersonic Inlet Systems," AIAA Paper 84-0194, Jan. 1984.
9. Vakili, A., Wu, J. M., Bhat, M. K., Liver, P., Hingst, W. R., and Towne, C. E., "Comparison of Experimental and Computational Compressible Flow in an S-Duct," AIAA Paper 84-0033, Jan. 1984.
10. Rowe, M., "Measurements and Computations of Flow in Pipe Bends," Journal of Fluid Mechanics, Vol. 43, Pt. 4, Oct. 2, 1970, pp. 771-783.
11. Reyhner, T. A., and Flugge-Lotz, I., "The Interaction of a Shock Wave with a Laminar Boundary Layer," International Journal of Non-Linear Mechanics, Vol. 3, No. 2, June 1968, pp. 173-199.
12. Liu, N.-S., Shamroth, S. J., and McDonald, H., "Numerical Solution of Navier-Stokes Equations for Compressible Turbulent Two/Three Dimensional Flows in the Terminal Shock Region of an Inlet/Diffuser," NASA CR-3723, Aug. 1983.

ORIGINAL PAGE IS
OF POOR QUALITY

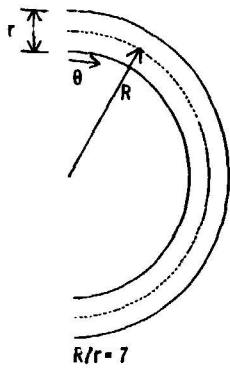


Figure 1. - 180 degree bend configurations.

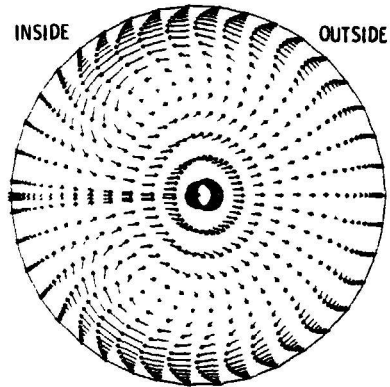
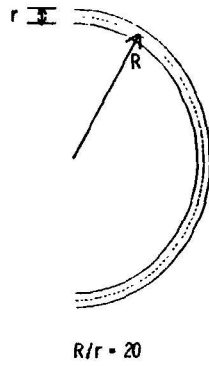


Figure 2. - Computed secondary flow at $\theta = 60^\circ$
in $R/r = 7$ duct.

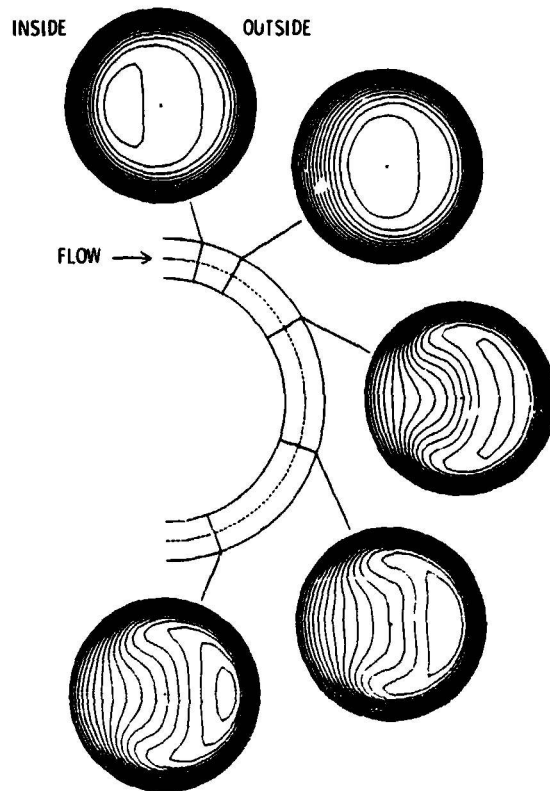


Figure 3. - Computed streamwise velocity contours in $R/r = 7$ duct.

ORIGINAL PAGE IS
OF POOR QUALITY

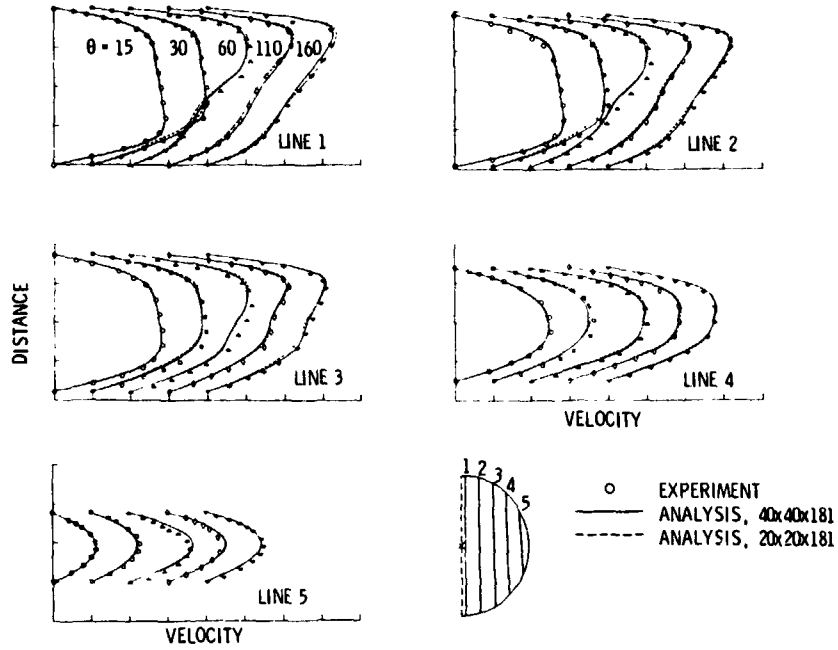


Figure 4 - Computed and experimental streamwise velocity profiles in $R/r = 7$ duct.

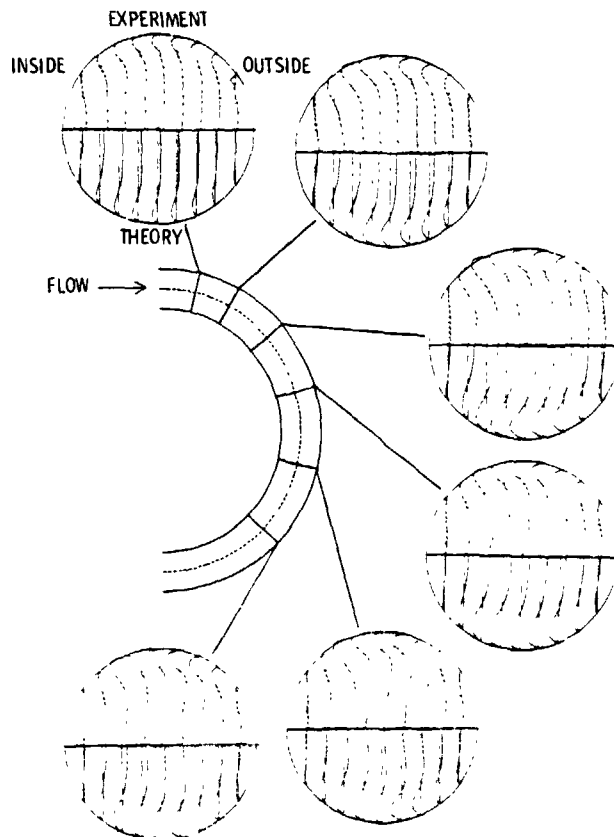


Figure 5 - Computed and experimental cross-flow velocity profiles in $R/r = 7$ duct.

ORIGINAL IMAGE IS
OF POOR QUALITY

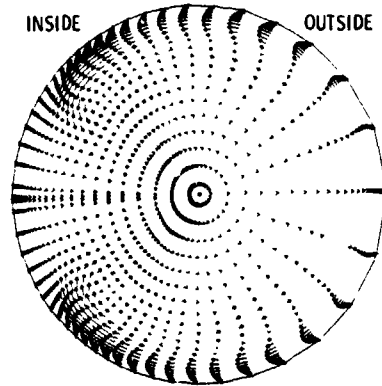


Figure 6. - Computed secondary flow at $\theta = 84^\circ$
in $R/r = 20$ duct.

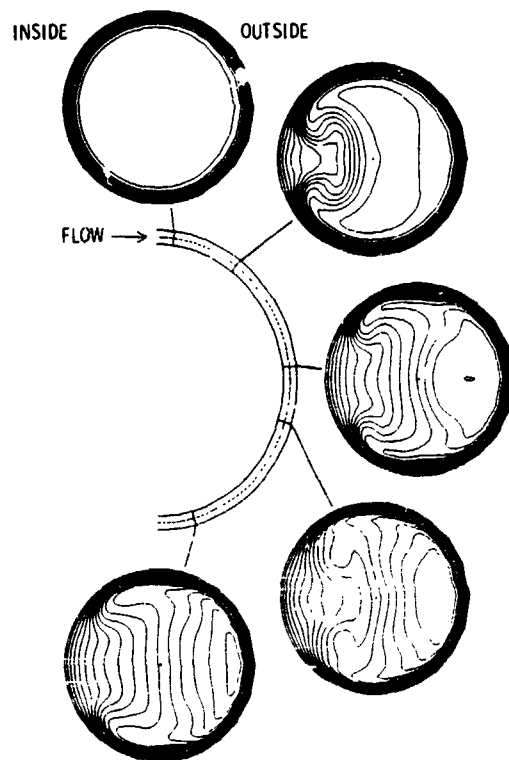
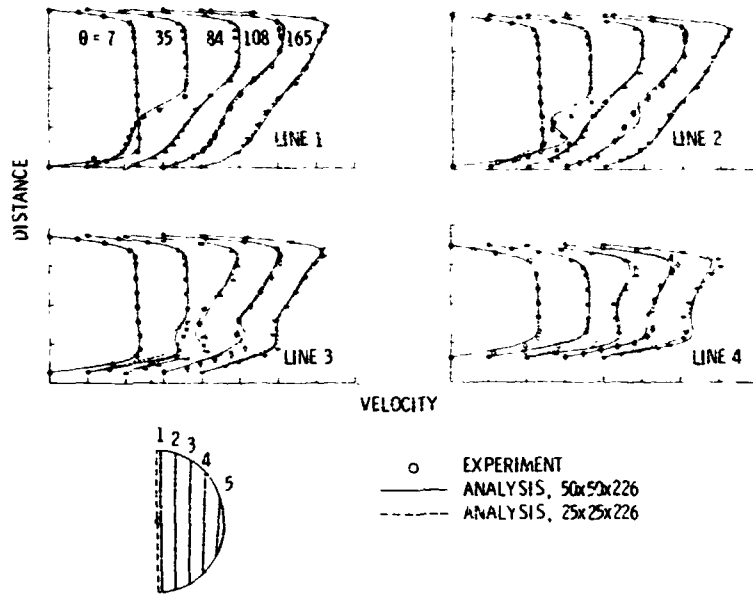


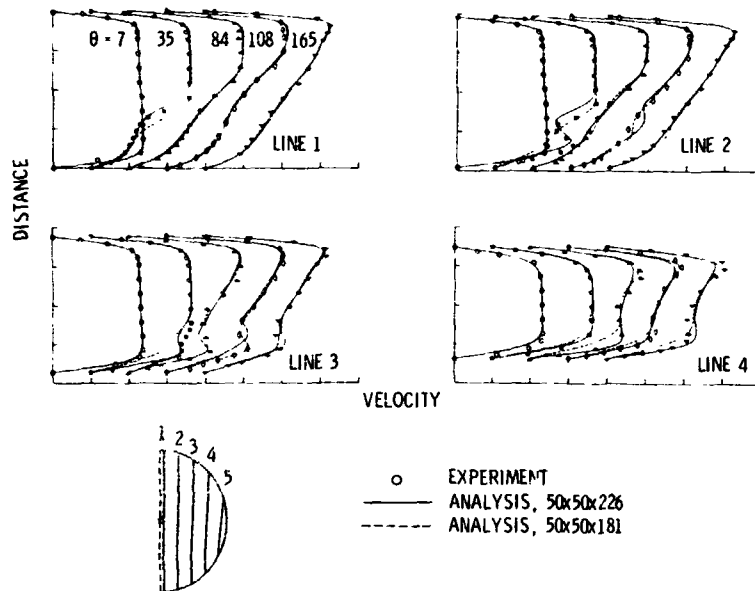
Figure 7. - Computed streamwise velocity contours in $R/r = 20$ duct.

COMPARISON OF
OF POOR QUALITY



(a) Effect of cross-sectional mesh.

Figure 8. - Computed and experimental streamwise velocity profiles in $R/r = 20$ duct.



(b) Effect of streamwise mesh.

Figure 8. - Concluded.

ORIGINAL PAGES 22
OF POOR QUALITY

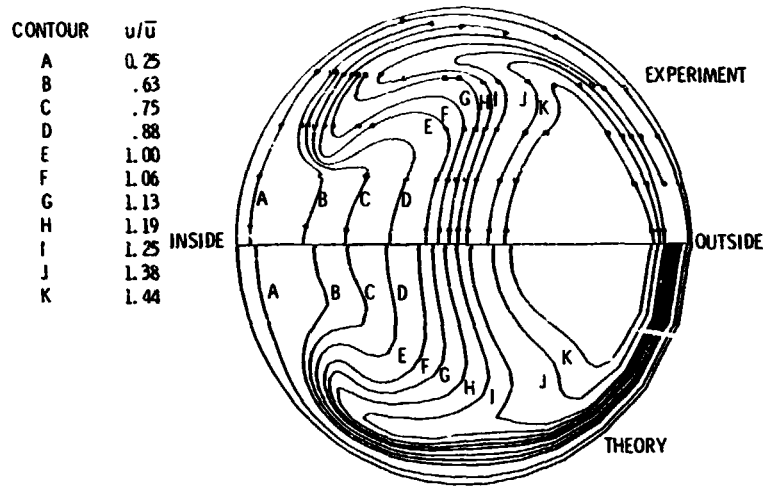


Figure 9. - Computed and experimental streamwise velocity contours at $\theta = 84^\circ$ in $R/r = 20$ duct.

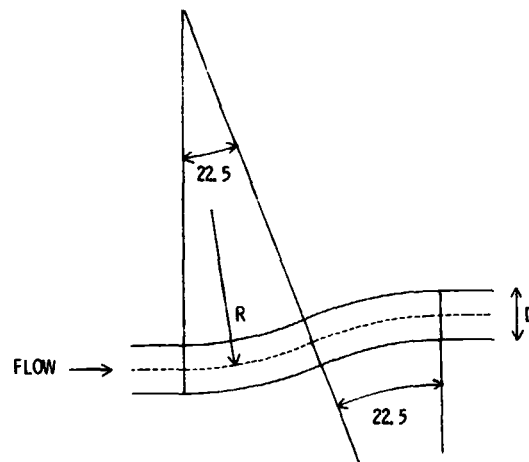


Figure 10. - S-duct configuration.

ORIGIN
OF POOR QUALITY

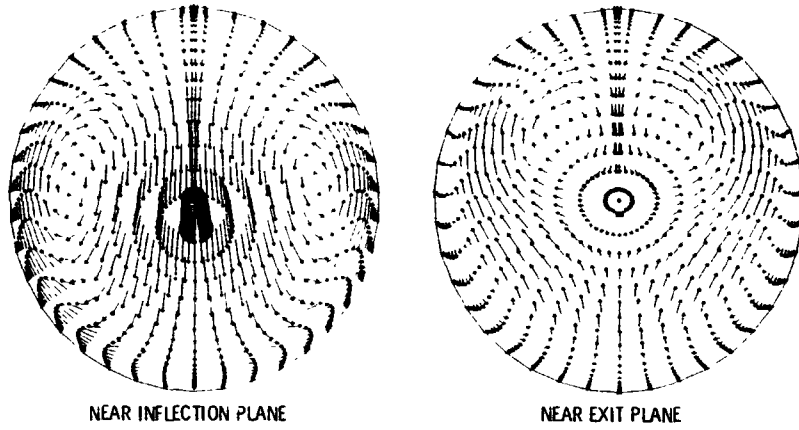
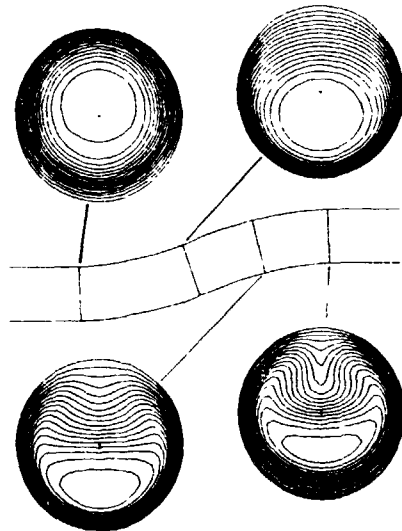


Figure 11. - Computed secondary velocities for laminar flow in 22.5-22.5 circular S-duct.



ORIGINAL PAGES OF POOR QUALITY

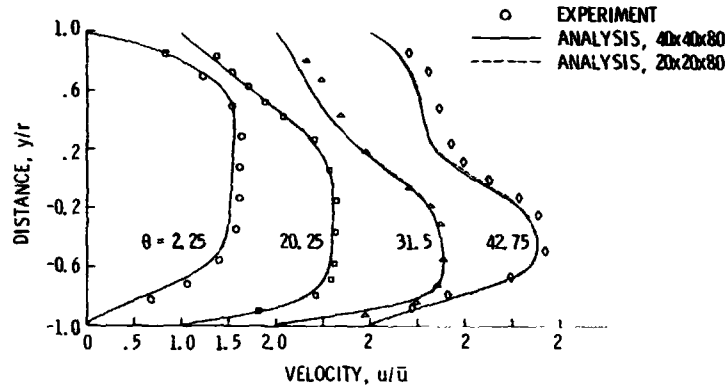


Figure 13. - Computed and experimental streamwise velocity profiles in symmetry plane for laminar flow in 22.5 - 22.5 circular S-duct.

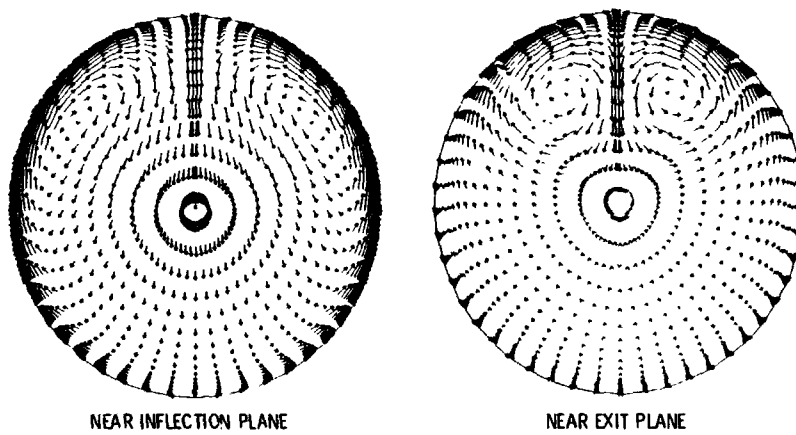


Figure 14. - Computed secondary velocities for turbulent flow in 22.5 - 22.5 circular S-duct.

ORIGINAL FIGURE
OF POOR QUALITY

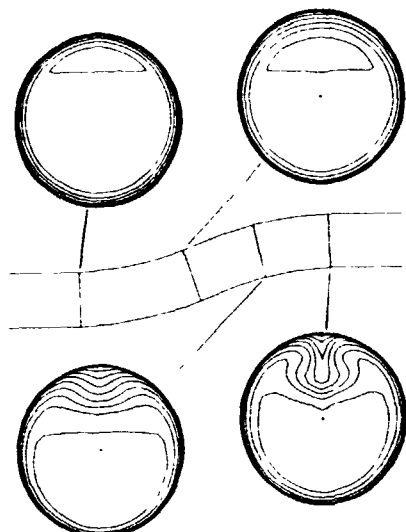


Figure 15. - Computed streamwise velocity contours for turbulent flow in 22.5 - 22.5 circular S-duct.

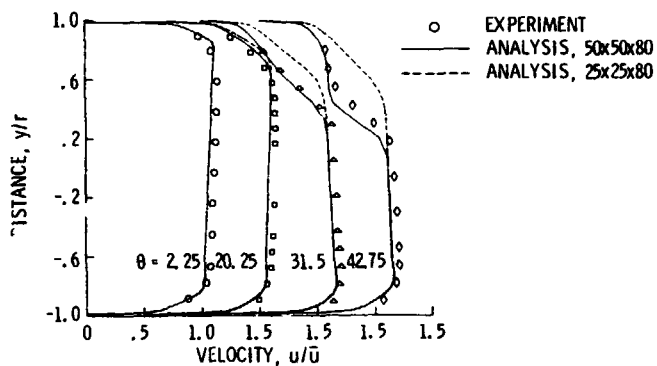


Figure 16. - Computed and experimental streamwise velocity profiles in symmetry plane for turbulent flow in 22.5 - 22.5 circular S-duct.

ORIGINAL FIGURES
OF POOR QUALITY

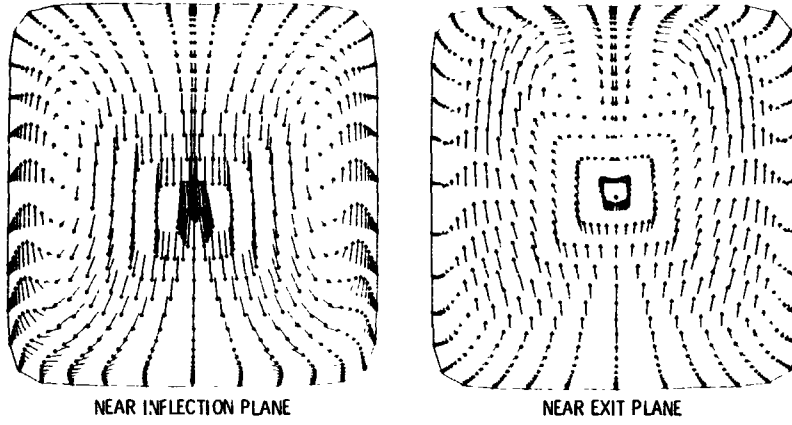


Figure 17. - Computed secondary velocities for laminar flow in 22.5 - 22.5 square S-duct.

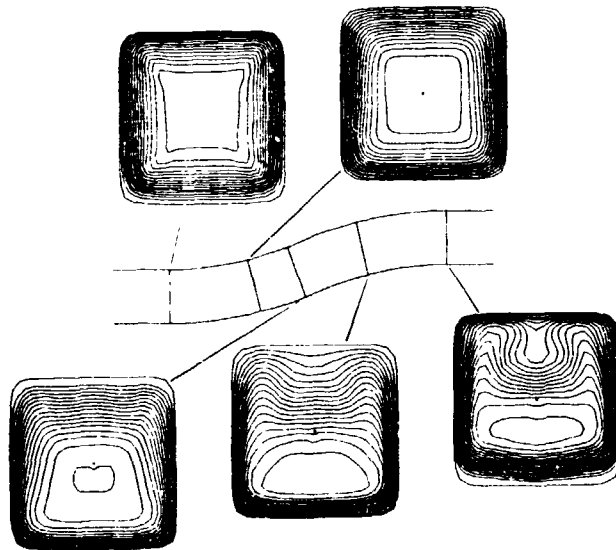


Figure 18. - Computed streamwise velocity contours for laminar flow in 22.5 - 22.5 square S-duct.

ORIGINAL PLOTS
OF POOR QUALITY

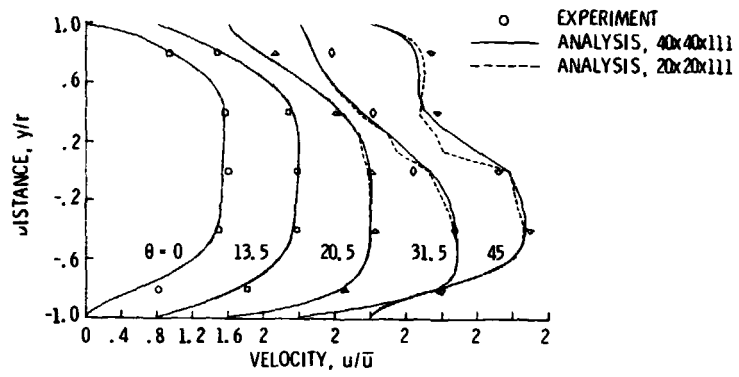


Figure 19. - Computed and experimental streamwise velocity profiles in symmetry plane for laminar flow in 22.5 - 22.5 square S-duct.

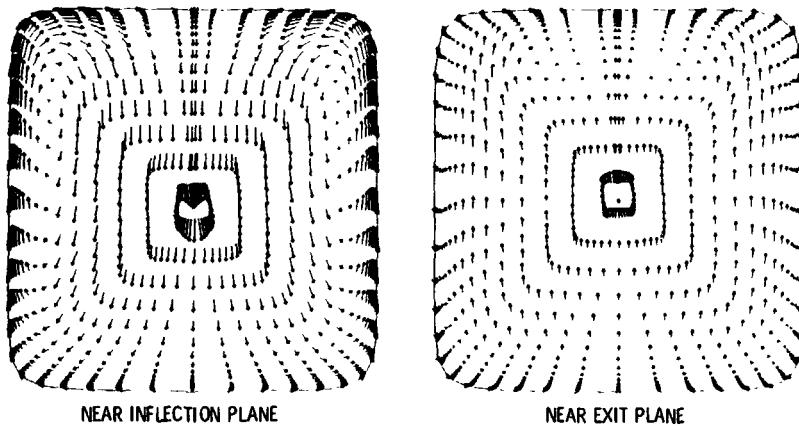


Figure 20. - Computed secondary velocities for turbulent flow in 22.5 - 22.5 square S-duct.

ORIGIN OF THE
OF POOR QUALITY

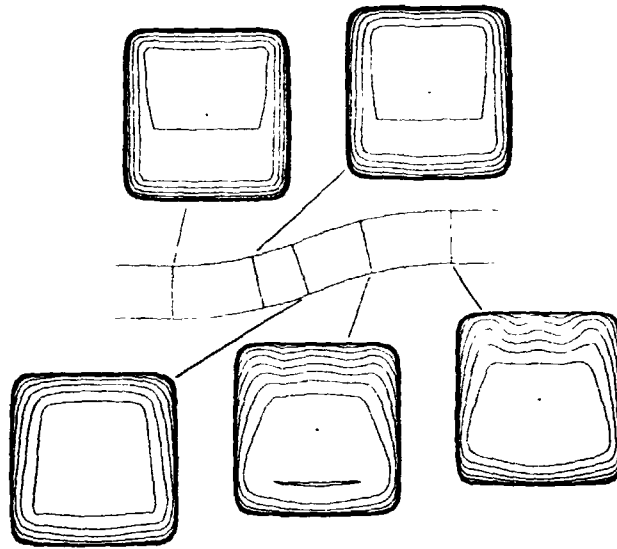


Figure 21. - Computed streamwise velocity contours for turbulent flow in 22.5 - 22.5 square S-duct.

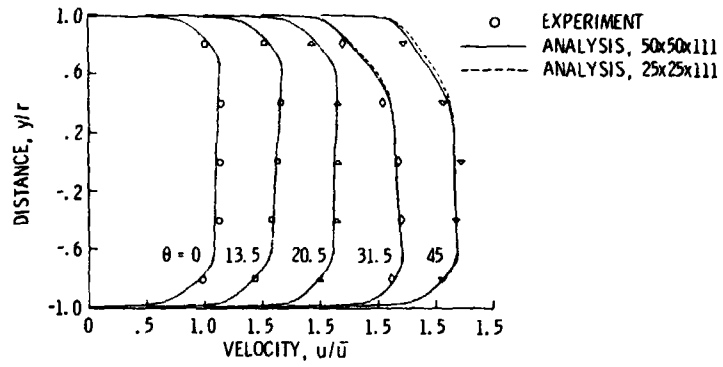


Figure 22. - Computed and experimental streamwise velocity profiles in symmetry plane for turbulent flow in 22.5 - 22.5 square S-duct.